The Astrophysical Journal, 977:98 (13pp), 2024 December 10 https://doi.org/10.3847/1538-4357/ad8cd8

NEOWISE-R Caught the Luminous SN 2023ixf in Messier 101

Schuyler D. Van Dyk[1], Tamás Szalai[2,3], Roc M. Cutri[1], J. Davy Kirkpatrick[1], Carl J. Grillmair[4], Sergio B. Fajardo-Acosta[1], Joseph R. Masiero[1], Amy K. Mainzer[5,6], Christopher R. Gelino[1], József Vinkó[2,7,8,9], András Péter Joó[7,8,9], András Pál[7,8], Réka Könyves-Tóth[2,7,8,10], Levente Kriskovics[7,8], Róbert Szakáts[7,8], Krisztián Vida[7,8], WeiKang Zheng[11], Thomas G. Brink[11], and Alexei V. Filippenko[11]
[1] Caltech/IPAC, Mailcode 100-22, Pasadena, CA 91125, USA; vandyk@ipac.caltech.edu
[2] Department of Experimental Physics, Institute of Physics, University of Szeged, Dóm tér 9, Szeged, 6720, Hungary
[3] MTA-ELTE Lendület "Momentum" Milky Way Research Group, Hungary
[4] Caltech/IPAC, Mailcode 314-6, Pasadena, CA 91125, USA
[5] University of Arizona, 1629 E. University Boulevard, Tucson, AZ 85721, USA
[6] Department of Earth, Planetary, and Space Sciences, The University of California, Los Angeles, 595 Charles E. Young Drive East, Los Angeles, CA 90095, USA
[7] HUN-REN CSFK Konkoly Observatory, Konkoly Th. M. út 15-17, Budapest, 1121, Hungary
[8] CSFK, MTA Centre of Excellence, Konkoly Thege Miklós út 15-17, Budapest, 1121, Hungary
[9] ELTE Eötvös Loránd University, Institute of Physics and Astronomy, Pázmány Péter sétány 1/A, Budapest, 1117, Hungary
[10] ELTE Eötvös Loránd University, Gothard Astrophysical Observatory, Szombathely, Hungary
[11] Department of Astronomy, University of California, Berkeley, CA 94720-3411, USA
Received 2024 June 25; revised 2024 October 8; accepted 2024 October 28; published 2024 December 5

Abstract

During routine survey imaging, the reactivated Near-Earth Object Wide-field Infrared Survey Explorer (NEOWISE-R) serendipitously caught the Type II supernova SN 2023ixf in Messier 101 on the rise, starting day 3.6 through day 10.9, and again on the decline at late times from days 211 through 213 and days 370 through 372. We have considered these mid-IR data together with observations from the ultraviolet (UV) through the near-IR, when possible. At day 3.6 we approximated the optical emission with a hot, ∼26,630 K blackbody, with a notable UV excess inferred to result from strong supernova (SN) shock interaction with circumstellar matter (CSM). In the IR, however, a clear excess is also obvious, and we fit it with a cooler, ∼1620 K blackbody with a radius of $\sim 2.6 \times 10^{15}$ cm, consistent with dust in the progenitor's circumstellar shell likely heated by the UV emission from the CSM interaction. On day 10.8, the light detected was consistent with SN ejecta-dominated emission. At late times we also observed a clear NEOWISE-R excess, which could arise either from newly formed dust in the inner ejecta or in the contact discontinuity between the forward and reverse shocks, or from more distant pre-existing dust grains in the SN environment. Furthermore, the large 4.6 μm excess at late times can also be explained by the emergence of the carbon monoxide 1–0 vibrational band. SN 2023ixf is the best-observed SN II in the mid-IR during the first several days after the explosion and one of the most luminous such SNe ever seen.

Unified Astronomy Thesaurus concepts: Supernovae (1668); Core-collapse supernovae (304); Type II supernovae (1731); Dust formation (2269); Circumstellar dust (236)

1. Introduction

Supernova (SN) explosions are among the most powerful events in the Universe. They serve as unique cosmic laboratories for studying processes in extreme physical conditions and chemical feedback into the interstellar and intergalactic media. Core-collapse supernovae (CCSNe), consequences of the gravitational collapse of iron cores of massive ($\gtrsim 8\,M_\odot$) stars, have been considered possible sources of cosmic dust at high redshifts for over ∼50 yr (e.g., F. Cernuschi & S. Codina 1967; F. Hoyle & N. C. Wickramasinghe 1970; E. Dwek et al. 2007). Observed dust in CCSNe may form either in the (unshocked) ejecta or in a cold, dense shell (CDS) across the contact discontinuity between the shocked circumstellar matter (CSM) and shocked ejecta. A late-time mid-IR excess may emerge from either newly formed or heated pre-existing dust grains. In the shocked CSM, heating can be collisional, and grains in the more distant, unshocked CSM are assumed to be radiatively heated by the peak SN luminosity or by energetic photons generated during CSM interaction (see, e.g., C. Gall et al. 2011 for a review).

Observed properties and classifications of CCSNe, from H-rich to H-free spectra (in the classical scheme of IIP, IIL, IIb, to Ib/c; see A. V. Filippenko 1997 and A. Gal-Yam 2017 for reviews), depend mainly on the degree of pre-explosion mass loss from the progenitor star (and/or its companion in a binary system). H-rich Type II-plateau (IIP) SNe, characterized by their ∼100 days optical plateau-like light curves, are the predominant CCSN subclass (corresponding to ∼55% of all CCSNe; D. A. Perley et al. 2020). Direct evidence exists that these SNe arise from stars in the red supergiant (RSG) phase, with the star's massive hydrogen envelope remaining relatively intact at explosion (S. J. Smartt et al. 2009; S. J. Smartt 2015; S. D. Van Dyk 2017). SNe IIP are known to form new dust in their ejecta (see C. Gall et al. 2011 and references therein). Based on recent model calculations, expanding SN IIP ejecta succeeds in condensing sufficient quantities (0.05–1.0 $M_\odot$) of dust. Some of these models propose slow and steady dust growth over several thousand days (e.g., C. Gall et al. 2014; R. Wesson et al. 2015), while others suggest a more rapid dust growth (E. Dwek et al. 2019; A. Sarangi 2022). These theoretical expectations are also in agreement with the far-IR/submillimeter detection of a

large amount of cold ($\lesssim$50 K) dust in hundreds of years old Galactic SN remnants, such as Cas A (M. J. Barlow et al. 2010; B. Sibthorpe et al. 2010; R. G. Arendt et al. 2014) and the Crab Nebula (H. L. Gomez et al. 2012; T. Temim & E. Dwek 2013; I. De Looze et al. 2019), as well as the nearby (∼50 kpc) and famous SN 1987A (M. Matsuura et al. 2011; R. Indebetouw et al. 2014; M. Matsuura et al. 2019). Very recently, the James Webb Space Telescope (JWST) has offered a new opportunity to study the late phases of cool (∼100–200 K) dust in extragalactic SNe and has already led to the detection of a significant amount ($\gtrsim 10^{-3}\,M_{\odot}$) of dust in the luminous Type IIP SNe 2004et and 2017eaw (M. Shahbandeh et al. 2023), and the Type II-linear (IIL) SN 1980K (S. Zsíros et al. 2024).

At the same time, only a handful of nearby young ($\lesssim$5 yr) SNe II (primarily IIP) show direct observational evidence for dust condensation, and these examples have all yielded 2–3 orders of magnitude less dust ($\sim 10^{-5}$–$10^{-3}\,M_{\odot}$) than predicted by the models. Most of these observations, however, were carried out in the wavelength range 3–5 μm and thus have been limited to just the warmer ($\gtrsim$500 K) dust grains. In the last quarter century, the primary source of mid-IR data on SNe was NASA's Spitzer Space Telescope, which resulted in valuable data during both its cryogenic (2003–2009) and postcryogenic (2009–2020) missions. Except for several single-object studies—e.g., SN 1987A (P. Bouchet et al. 2006; E. Dwek et al. 2010), SN 1993J (S. Zsíros et al. 2022), SN 1995N (S. D. Van Dyk 2013), SN 2003gd (B. E. K. Sugerman et al. 2006; W. P. S. Meikle et al. 2007), SN 2004dj (W. P. S. Meikle et al. 2011; T. Szalai et al. 2011), SN 2004et (R. Kotak et al. 2009; J. Fabbri et al. 2011), SN 2005af (R. Kotak et al. 2006; T. Szalai & J. Vinkó 2013), SN 2005ip (O. D. Fox et al. 2010), SN 2007it (J. E. Andrews et al. 2011), and SN 2007od (J. E. Andrews et al. 2010)—most of these Spitzer SN data were collected in the postcryogenic phase (at 3.6 and 4.5 μm). Studies during this phase included either targeted surveys, such as the SPIRITS project (SPitzer InfraRed Intensive Transients Survey, a systematic study of transients in nearby galaxies; see S. Tinyanont et al. 2016; M. M. Kasliwal et al. 2017; J. E. Jencson et al. 2019) and work focused on interacting SNe (O. D. Fox et al. 2011, 2013; T. Szalai et al. 2021), or archival images for which the SNe were not the primary target (T. Szalai et al. 2019). The latter work, including data from targeted surveys, presents the most extensive analysis of mid-IR SN observations to date, including ∼120 positively detected objects from ∼1100 SN sites imaged by Spitzer.

Another very important tool for detecting early-time mid-IR radiation from SNe has been the Wide-field Infrared Survey Explorer (WISE, both cryogenic and postcryogenic, 2009–2011; E. L. Wright et al. 2010). The postcryogenic WISE mission was reactivated in 2013 and had been monitoring the sky at 3.4 and 4.6 μm ever since, as the Near-Earth Object Wide-field Infrared Survey Explorer Reactivation (NEOWISE-R, or NEOWISE for short; A. Mainzer et al. 2011, 2014). While the original aim of the reactivated mission was mainly characterization of known solar system objects, its archive also serves as a valuable source of information on a rich variety of transient objects, such as cataclysmic variables, active galactic nuclei, tidal disruption events, and SNe (e.g., M. Kokubo et al. 2019; L. Tartaglia et al. 2020; L. Sun et al. 2022; S. Moran et al. 2023; L. Wang et al. 2024).

We as a community have been incredibly fortunate to have the recent, nearby SN 2023ixf occur in Messier 101 (M101; NGC 5457). Its proximity and brightness have led to many investigators training various facilities at a range of wavelengths at the event, which has exhibited a number of fascinating properties. The SN was discovered by K. Itagaki (2023) on 2023 May 19.73 (UTC dates are used throughout this paper) and classified as an SN II by D. A. Perley et al. (2023) within hours of discovery. It was evident immediately that the optical spectrum was dominated by "flash" emission features indicative of interaction of the SN shock with pre-existing CSM (e.g., K. A. Bostroem et al. 2023; D. Hiramatsu et al. 2023; W. V. Jacobson-Galán et al. 2023; R. S. Teja et al. 2023). The SN's light curves provided similar indications (e.g., D. Hiramatsu et al. 2023; G. Hosseinzadeh et al. 2023; L. Martinez et al. 2024). E. A. Zimmerman et al. (2024), from an analysis of early-time Hubble Space Telescope (HST) ultraviolet (UV) spectroscopy of the SN, constrained the CSM to be dense and confined, with $\sim 10^{-12}$ g cm^{-3} at $\lesssim 2 \times 10^{14}$ cm; they concluded that this dense CSM immediate to the progenitor prolonged the SN shock breakout by ∼3 days. Other indications of initial and longer-term CSM interaction for SN 2023ixf come from observations at X-ray (B. W. Grefenstette et al. 2023; P. Chandra et al. 2024) and radio (E. Berger et al. 2023) wavelengths.

The strict subclassification of SN 2023ixf is not widely agreed upon. The distinction between the IIP and IIL subtypes has been classically established based on light-curve shape and the duration of a plateau phase (R. Barbon et al. 1979), although spectroscopic differences in the Balmer line profiles also may be apparent (E. M. Schlegel 1996). However, it has been argued that SN IIL light curves may not be stringently distinguished from those of SNe IIP (J. P. Anderson et al. 2014; S. Valenti et al. 2016). Y.-P. Yang et al. (2024) observed a significant drop from the plateau for the SN 2023ixf light curves between 59 and 90 days. Similarly, A. Singh et al. (2024) found that the SN began to fall from the plateau in the V band at ∼75 days, to the exponential tail at ∼90 days, at the shorter end of the typical SN IIP plateau duration. Those authors noted that SN 2023ixf therefore resembles several "short-plateau" SNe IIP (D. Hiramatsu et al. 2021; R. S. Teja et al. 2022); see also B. Hsu et al. (2024). K. A. Bostroem et al. (2023, 2024) and Y. Dong et al. (2023) have referred to the SN as IIP/L. S. D. Van Dyk et al. (2024) considered SN 2023ixf as a short-plateau IIP or IIP/IIL hybrid. Hereafter, we will categorize the SN based on its original D. A. Perley et al. (2023) classification as SN II.

A progenitor candidate was directly identified in archival HST, Spitzer, and ground-based near-IR data (e.g., J. E. Jencson et al. 2023; C. D. Kilpatrick et al. 2023; J. L. Pledger & M. M. Shara 2023; M. D. Soraisam et al. 2023; S. D. Van Dyk et al. 2024). These unprecedented data were plentiful enough that the star was shown in astonishing detail to be a long-period variable, similar to what we expect for many RSGs (J. E. Jencson et al. 2023; M. D. Soraisam et al. 2023). Additionally, modeling of the star's spectral energy distribution (SED), e.g., by S. D. Van Dyk et al. (2024), revealed it to be quite dusty and luminous and implied that the star was surrounded by a dusty silicate-rich shell with an inner radius of ≈10 times the star's radius, or $\approx 10^{15}$ cm.

Near-IR studies of SN 2023ixf have already been conducted and published (R. S. Teja et al. 2023; M. Yamanaka et al. 2023), and others will likely emerge. The SN has already been observed with the JWST, and those results are pending. Here we describe and analyze observations by NEOWISE, which serendipitously caught SN 2023ixf in the act between ∼3 days and ∼372 days of age. This is among the earliest that an SN has been detected in the mid-IR (the peculiar Type IIP SN 2009js

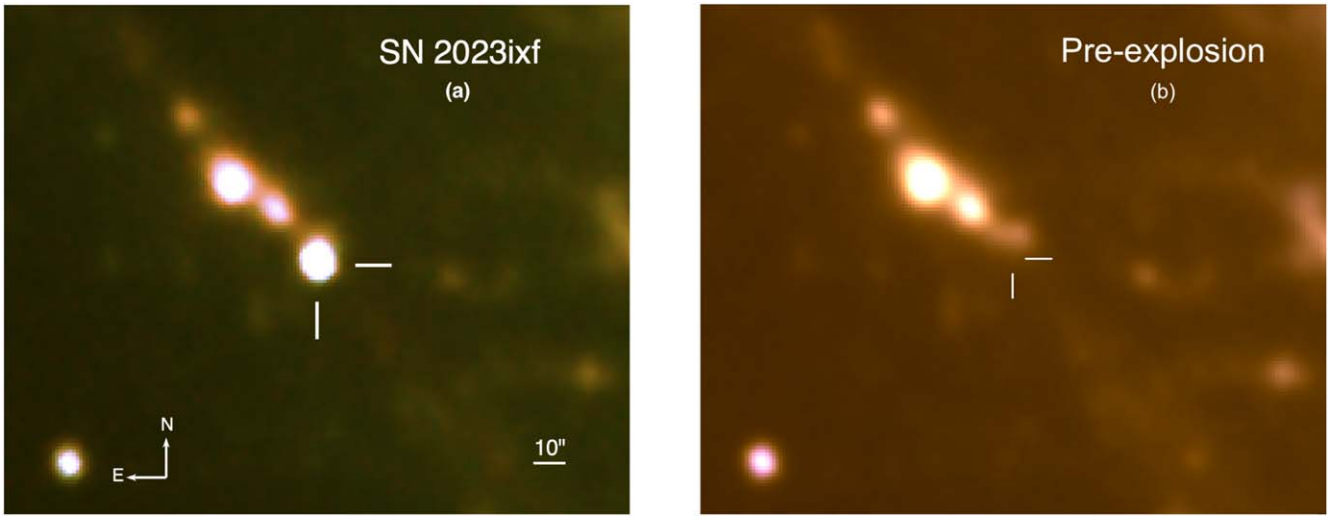

Figure 1. (a) Color-composite image of the NEOWISE-R detection of SN 2023ixf in M101 at 3.4 and 4.6 μm (bands W1 and W2, respectively) in the day 3.361–4.995 range combined using `ICORE` (see Table 1). The SN is indicated with tick marks. The bright emission to the northeast of the SN is from the giant H II region complex NGC 5461. (b) Color-composite deep stack of all of the NEOWISE-R frames in bands W1 and W2 obtained prior to explosion (see Appendix) to approximately the same scale and orientation of the left panel. The SN position is indicated with tick marks.

was caught by Spitzer two days after discovery; however, its explosion epoch is rather uncertain; P. Gandhi et al. 2013; T. Szalai et al. 2019).

Following G. Hosseinzadeh et al. (2023), we have adopted 2023 May 18 at 18:00 UTC (MJD 60082.75) as the explosion epoch. We assume throughout a distance to M101 of 6.85 ± 0.13 Mpc (A. G. Riess et al. 2022).

2. Observations

2.1. NEOWISE

NEOWISE observed the SN site pre-explosion, as part of routine operations, 152 times between 2013 December 18.26 and 2022 December 18.99 UT (MJD 56644.2618 and 59931.9958, respectively). The first pre-SN pair of single exposures occurred 3438.49 days prior to the explosion, while the last was 150.75 days pre-SN. The progenitor candidate was not detected in any of these observations (e.g., D. Hiramatsu et al. 2023; J. E. Jencson et al. 2023; M. D. Soraisam et al. 2023; S. D. Van Dyk et al. 2024). See also the Appendix of this paper. The lack of detection tends to rule out luminous eruptions or outbursts from the progenitor candidate during that time period prior to the explosion, as discussed in the above studies. (The star was also not detected by WISE and the postcryogenic NEOWISE prior to reactivation between 2009 and 2011; see S. D. Van Dyk et al. 2024.)

The SN itself was detected during the 19th sky coverage since the start of the Reactivation Mission, from day 3.631 through 10.901 (2023 May 22.38 through May 29.65). We note that the gap of several days in the early-time data is caused by a "Moon toggle" procedure, in which the spacecraft pointing skips ahead to avoid the Moon and then slews back to observe the "skipped" area of sky (see E. L. Wright et al. 2010 for a description); in our case, this was advantageous, as we were able to sample the SN's evolution about a week after the first detections. All of these data (NEOWISE Team 2020) are publicly available via the NASA/IPAC Infrared Science Archive[12]; see Figure 1. The SN was then captured again at late times during the 21st sky coverage, from day 211.736 through 213.351 (2023 December 16.49 through 18.10), and then again from day 370.875 through 372.476 (2024 May 23.63 through 25.23). Those data were still prerelease at the time of this writing and were also obtained via IRSA. (Those data have since all been publicly released.) Given the separation of the SN from the general environs of the neighboring giant H II region NGC 5461, the detections are relatively clean. The SN detections are listed in Table 1. The quantities `W1mpro`and `W2mpro` are profile-fit photometry magnitudes at 3.4 and 4.6 μm (bands W1 and W2), respectively, in the Vega system,[13] without any further special processing or additional background subtraction applied. However, the magnitudes have been corrected for variations in the system throughput (sensitivity) as a function of MJD (scan) and boresight assembly temperature of the spacecraft.[14] The resulting light curves are shown in Figure 2.

2.2. Late-time Optical Data

2.2.1. Konkoly Observatory

Many investigators have continued to follow SN 2023ixf since its discovery. We (Vinkó Joó Pál, Kriskovics, Könyves-Tóth, Szakáts, Vida) obtained optical photometry with the 0.8 m Ritchey–Chrétien telescope at the Konkoly Observatory, Hungary (J. Vinkó et al. 2024, in preparation). This includes late-time Johnson *BV* and Sloan Digital Sky Survey (SDSS) *g'r'i'z'* (hereafter *BVgriz*) photometry from MJD 60297.0 (2023 December 18.5, day 214) and from MJD 60444.93 (2024 May 14.9, day 362.18). These data were processed with standard IRAF[15] routines. Photometric calibration was based on field stars in the Pan-STARRS DR1 (PS1) catalog[16]

[12] IRSA, https://irsa.ipac.caltech.edu/.

[13] See the NEOWISE Data Release Explanatory Supplement, https://wise2.ipac.caltech.edu/docs/release/neowise/expsup/.

[14] https://wise2.ipac.caltech.edu/docs/release/neowise/expsup/sec4_2d.html

[15] IRAF is distributed by the National Optical Astronomy Observatories, which are operated by the Association of Universities for Research in Astronomy, Inc., under a cooperative agreement with the National Science Foundation.

[16] https://catalogs.mast.stsci.edu/panstarrs/

Table 1
NEOWISE-R Observations of SN 2023ixf

MJD	Age (day)	Scan ID	Frame Num	W1mpro (mag)	W1sigmpro (mag)	W2mpro (mag)	W2sigmpro (mag)
60086.381	3.631	50719r	232	11.348	0.020	11.276	0.026
60086.511	3.761	50723r	159	11.298	0.022	11.252	0.036
60086.641	3.891	50727r	232	11.292	0.019	11.202	0.028
60086.771	4.021	50731r	232	11.238	0.020	11.299	0.026
60086.836	4.086	50733r	207	11.275	0.021	11.222	0.026
60086.836	4.086	50733r	208	11.273	0.023	11.285	0.027
60086.901	4.151	50735r	231	11.222	0.020	11.172	0.028
60086.966	4.216	50737r	207	11.244	0.019	11.210	0.031
60087.031	4.281	50739r	232	11.256	0.018	11.136	0.025
60087.096	4.346	50741r	208	11.254	0.020	11.207	0.028
60087.160	4.410	50743r	157	11.205	0.018	11.187	0.026
60087.225	4.475	50745r	157	11.242	0.021	11.145	0.025
60087.290	4.540	50747r	232	11.224	0.018	11.166	0.026
60087.355	4.605	50749r	208	11.218	0.020	11.185	0.026
60087.420	4.670	50751r	232	11.197	0.020	11.159	0.026
60087.484	4.734	50753r	157	11.351	0.020	11.440	0.027
60087.485	4.735	50753r	158	11.205	0.020	11.169	0.032
60087.549	4.799	50755r	156	11.205	0.017	11.104	0.023
60087.615	4.865	50757r	208	11.192	0.020	11.152	0.028
60087.680	4.930	50759r	232	11.177	0.018	11.128	0.023
60087.745	4.995	50761r	207	11.142	0.021	11.101	0.023
60087.745	4.995	50761r	208	11.142	0.021	11.154	0.026
60087.874	5.124	50765r	207	11.169	0.018	11.148	0.024
60088.004	5.254	50769r	208	11.143	0.017	11.172	0.024
60088.134	5.384	50773r	156	11.114	0.019	11.084	0.022
60093.586	10.836	50941r	211	10.715	0.019	10.712	0.021
60093.651	10.901	50942r	235	10.684	0.016	10.634	0.020
60294.486	211.736	57146r	007	11.918	0.027	10.535	0.020
60294.616	211.866	57150r	042	11.917	0.021	10.496	0.018
60294.745	211.995	57154r	042	11.892	0.021	10.479	0.019
60294.874	212.124	57158r	042	11.876	0.020	10.503	0.018
60294.938	212.188	57160r	017	11.846	0.020	10.505	0.018
60295.003	212.253	57162r	042	11.888	0.022	10.484	0.018
60295.068	212.318	57164r	018	11.927	0.023	10.474	0.019
60295.197	212.447	57168r	018	11.837	0.020	10.501	0.019
60295.261	212.511	57170r	042	11.873	0.023	10.562	0.025
60295.326	212.576	57172r	018	11.857	0.020	10.503	0.018
60295.390	212.640	57174r	042	11.926	0.024	10.501	0.021
60295.455	212.705	57176r	017	11.899	0.021	10.487	0.019
60295.584	212.834	57180r	017	11.869	0.023	10.471	0.020
60295.649	212.899	57182r	042	11.908	0.025	10.507	0.021
60295.713	212.963	57184r	018	11.928	0.023	10.522	0.019
60295.778	213.028	57186r	043	11.922	0.028	10.489	0.020
60295.842	213.092	57188r	018	11.902	0.024	10.518	0.020
60295.972	213.222	57192r	018	11.891	0.023	10.517	0.023
60296.101	213.351	57196r	018	11.937	0.024	10.494	0.020
60453.625	370.875	62087r	131	13.136	0.038	11.775	0.036
60453.753	371.003	62091r	231	13.114	0.034	11.791	0.039
60453.881	371.131	62095r	232	13.171	0.036	11.834	0.040
60453.945	371.195	62101r	206	13.189	0.035	11.720	0.039
60454.009	371.259	62103r	231	13.151	0.035	11.845	0.036
60454.073	371.323	62105r	232	13.091	0.032	11.745	0.037
60454.137	371.387	62107r	134	13.095	0.032	11.795	0.043
60454.201	371.451	62109r	135	13.168	0.038	11.754	0.038
60454.265	371.515	62111r	231	13.142	0.036	11.726	0.034
60454.329	371.579	62113r	206	13.258	0.038	11.812	0.037
60454.393	371.643	62115r	231	13.079	0.031	11.837	0.043
60454.457	371.707	62117r	205	13.084	0.049	11.751	0.032
60454.458	371.708	62117r	206	13.127	0.036	11.820	0.038
60454.521	371.771	62119r	231	13.111	0.032	11.792	0.041
60454.585	371.835	62121r	205	13.074	0.038	11.775	0.036
60454.650	371.900	62123r	231	13.161	0.032	11.792	0.033
60454.714	371.964	62125r	206	13.159	0.033	11.816	0.040

Table 1
(Continued)

MJD	Age (day)	Scan ID	Frame Num	W1mpro (mag)	W1sigmpro (mag)	W2mpro (mag)	W2sigmpro (mag)
60454.778	372.028	62127r	231	13.050	0.031	11.764	0.034
60454.842	372.092	62129r	206	13.248	0.036	11.683	0.038
60454.906	372.156	62131r	231	13.047	0.031	11.796	0.031
60454.970	372.220	62133r	206	13.222	0.035	11.774	0.041
60455.097	372.347	62137r	125	13.114	0.034	11.745	0.036
60455.226	372.476	62141r	206	13.195	0.035	11.799	0.035

Note. The columns W1mpro, W1sigmpro, W2mpro, and W2sigmpro are profile-fit photometry magnitudes and their uncertainties in the Vega system. The magnitudes have been corrected for variations in the system throughput as a function of boresight assembly temperature; see text.

(K. C. Chambers et al. 2016). In order to obtain reference magnitudes for our *B* and *V* frames, the PS1 magnitudes were transformed into the Johnson-Cousins *BVRI* system based on equations and coefficients provided by J. L. Tonry et al. (2012). Finally, the instrumental magnitudes were transformed into standard *BVgriz* magnitudes by applying a linear color term (using $g - i$) and wavelength-dependent zero-points. Since the reference stars were all within a few arcminutes around the SN, no atmospheric extinction correction was necessary.

2.2.2. Lick Observatory

We (Zheng, Brink, Filippenko) performed further follow-up *BVRI* photometric observations of SN 2023ixf with both the 0.76 m Katzman Automatic Imaging Telescope (KAIT) and the 1 m Nickel telescope, as well as spectroscopy with the Shane 3 m telescope at Lick Observatory; see W. Zheng et al. (2024, in preparation) for details of the observations and data reduction. Regarding the photometry, we isolated just the late-time data on MJD 60291.53 and 60303.59 (2023 December 13.53 and 25.59, or days 208.78 and 220.84, respectively), which bracketed the late-time NEOWISE observations and interpolated between these two sets of measurements. As far as spectroscopy, we have included spectra from Zheng et al. obtained on 60290.53 (2023 December 12.53, day 207.78) and 60445.41 (2024 May 15.41, day 362.66), which are the closest Lick spectra in time to the late-time NEOWISE observations.

3. Analysis

Throughout our analysis, we have assumed a total extinction to SN 2023ixf of $A_V = 0.12$ mag from S. D. Van Dyk et al. (2024). For UV through the near-IR, we adopted the E. L. Fitzpatrick (1999) reddening law. The extinction corrections for the NEOWISE bands are adopted from S. Wang & X. Chen (2019).

3.1. Early-time IR Emission

Rather than select every pair of observed NEOWISE W1 and W2 data points to analyze, for illustrative purposes, we have chosen to consider just two sets at early times, the very first one from MJD 60086.381 (day 3.631) and from 60093.586 (day 10.836). These adequately represent the two periods of early-time sampling of the light curves in these bands.

In order to put the NEOWISE data in context with the overall SED at these two epochs, we accumulated published light-curve data at UV, optical, and near-IR wavelengths corresponding to (or bracketing) the epochs. The data sources were then an amalgam of Swift UVW2, UVM2, UVW1 from E. A. Zimmerman et al. (2024), SDSS *ugriz* and Johnson $BVJHK_s$ from R. S. Teja et al. (2023), Johnson *UBV*, and SDSS *griz* from D. Hiramatsu et al. (2023), and Johnson *JHK* from M. Yamanaka et al. (2023).

Since the NEOWISE measurements are in the Vega system, the entirety of the data set presented by R. S. Teja et al. (2023), which is in the AB system, had to be converted to Vega magnitudes. The SDSS magnitudes from D. Hiramatsu et al. (2023) also required a similar conversion. No conversion was needed for the M. Yamanaka et al. (2023) *JHK* photometry. For day 3.631, the available UV–optical data were quasi-contemporaneous with the NEOWISE points; however, *JHK* required a linear interpolation between two bracketing epochs (the earlier epoch was at day 3.4, very close in time to NEOWISE). For day 10.836, none of the complementary data were contemporaneous, so we were forced to interpolate between bracketing epochs at all wavelengths.

The resulting SED is shown in Figure 3. In addition to the UV–optical photometric points, we included an FTN–FLOYDS-N spectrum of the SN obtained by K. A. Bostroem et al. (2023) on 2023 May 22, which we downloaded from WISeREP[17] (O. Yaron & A. Gal-Yam 2012). Both the spectrum and the photometry were first reddening corrected. This spectrum was further renormalized to the (dereddened) SN *V*-band brightness. As can be seen in the figure, the overall agreement is reasonable between the spectrum and the photometric points across the common wavelength range.

We then attempted to fit a single, simple blackbody to the SED at day 3.631. We found that a blackbody with $T_{\rm hot} = 26{,}630$ K provides a good fit to the optical data, although a clear excess exists in the UV relative to this fit. The fit implies that the SN luminosity at that epoch was $\gtrsim 4.1 \times 10^{43}$ erg s^{-1}; this is a lower limit, since there is clearly additional luminosity in the UV. This is consistent with the evidence for strong, early-time interaction of the SN shock with dense CSM (e.g., K. A. Bostroem et al. 2023; W. V. Jacobson-Galán et al. 2023; R. S. Teja et al. 2023; L. Martinez et al. 2024; E. A. Zimmerman et al. 2024); specifically, interaction in SNe II can strengthen the continuum flux and boost emission lines in the UV simultaneously (L. Dessart & D. J. Hillier 2022). The blackbody radius is then $R_{\rm hot} \approx 3.4 \times 10^{14}$ cm. The early-phase photometric and spectroscopic UV–optical SN observations provided evidence for strong interaction of the SN shock with a dense, confined ($<2 \times 10^{15}$ cm) CSM (e.g., K. A. Bostroem et al. 2023; W. V. Jacobson-Galán et al. 2023;

[17] https://www.wiserep.org

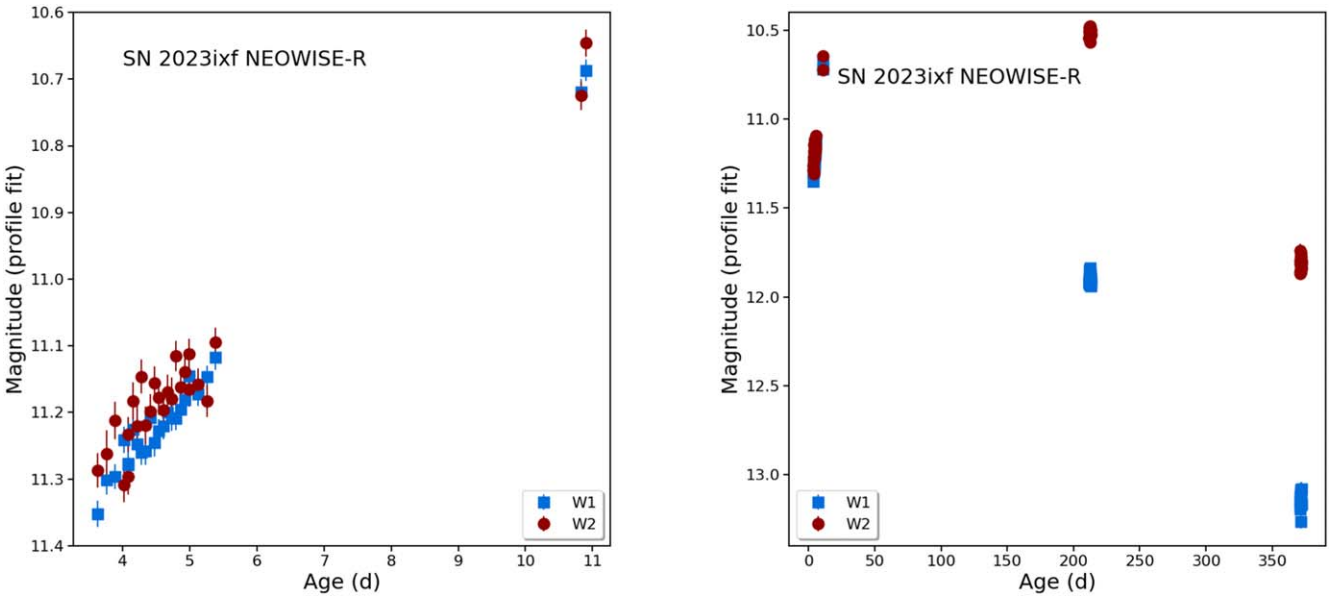

Figure 2. NEOWISE-R light curves of SN 2023ixf at 3.4 and 4.6 μm (bands W1 and W2, respectively). The observed magnitudes shown are in the Vega system (see Table 1). They have not been corrected for reddening. The left panel is limited to the early times between 3.631 and 10.901 days, in which the steady rise in the SN brightness is evident. The right panel shows the entire set of detections at both early and late times; for the latter, note the dramatic reddening in the color of the SN in the two bands at late times relative to the early times.

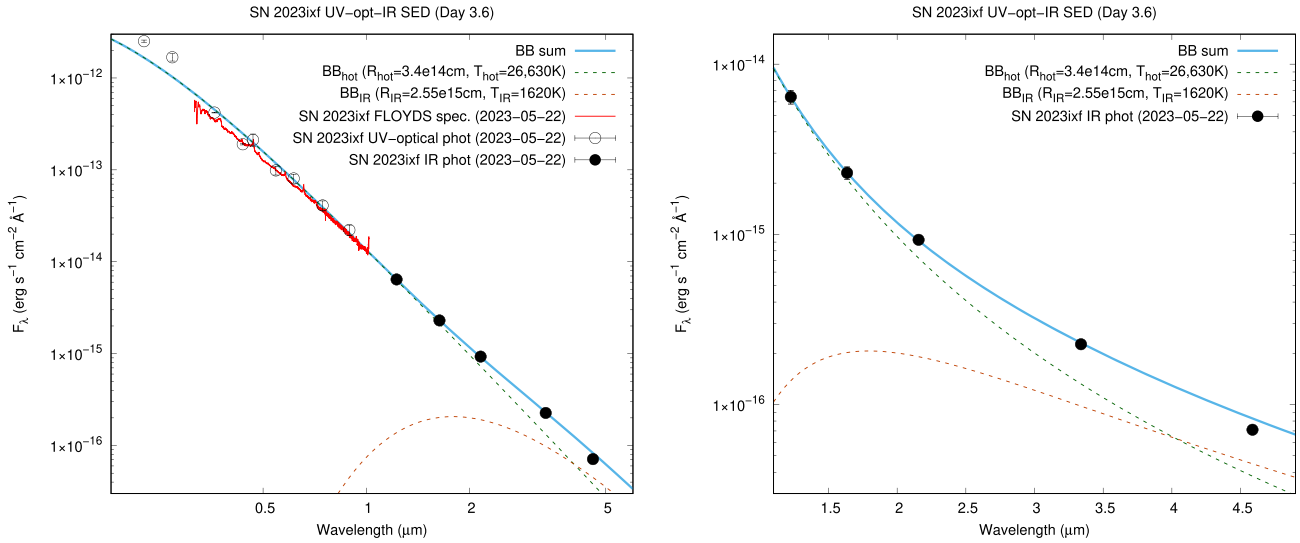

Figure 3. Left: the combined, dereddened UV–optical-IR SED of SN 2023ixf on day 3.6; see text for sources of the photometry. For comparison, we also show a dereddened, renormalized FTN/FLOYDS spectrum from day 3.54 (K. A. Bostroem et al. 2023, solid red curve). Blackbody SED fitting of only the near-IR and mid-IR fluxes (filled circles) required two components: One component consisting of a hot ($T_{\rm hot} = 26{,}630$ K) blackbody ("$BB_{\rm hot}$"; dashed green curve), and the other a cooler ($T_{\rm IR} = 1620$ K) blackbody ("$BB_{\rm IR}$"; dashed orange curve). The total fit is shown as the solid blue curve. The inferred radii of the blackbodies are $R_{\rm hot} \approx 3.4 \times 10^{14}$ and $R_{\rm IR} \approx 2.6 \times 10^{15}$ cm. Right: a zoom-in of just the IR portion of the SED.

N. Smith et al. 2023; R. S. Teja et al. 2023). E. A. Zimmerman et al. (2024) further refined the extent of the dense CSM to $R_{\rm CSM} \approx 2 \times 10^{14}$ cm and concluded that it actually delayed shock breakout (SBO) from hours after explosion to $\sim$3 days. In other words, the very first NEOWISE data were likely obtained within just hours after SBO, and the inferred $R_{\rm hot}$ is consistent with the shock, having already overrun the confinements of the dense CSM. In fact, following E. A. Zimmerman et al. (2024) and assuming an SN expansion velocity $v_{\rm exp} = 8000$ km s^{-1}, on day 3.631 the shock would have been at $R_{\rm shock} \sim 2.5 \times 10^{14}$ cm, roughly consistent with $R_{\rm hot}$ (if $v_{\rm exp}$ instead had been a somewhat higher, $\sim$11,000 km s^{-1}, the two radii, $R_{\rm shock}$ and $R_{\rm hot}$, would be in better agreement).

Particularly fascinating here is that an obvious excess in flux, relative to the hot blackbody, can be seen in Figure 3 at $\gtrsim$1.5 μm. We found that we could account for this IR excess with an additional, much cooler blackbody at $\sim$1620 K. Including this extra blackbody provides a reasonable fit to JHK_s and W1, although it does not quite fit W2 as well. This additional source of IR emission is of a comparatively far smaller luminosity, $\sim 3.2 \times 10^{40}$ erg s^{-1}, than the SN shock (it accounts for $\lesssim$0.1% of the total emission). The corresponding

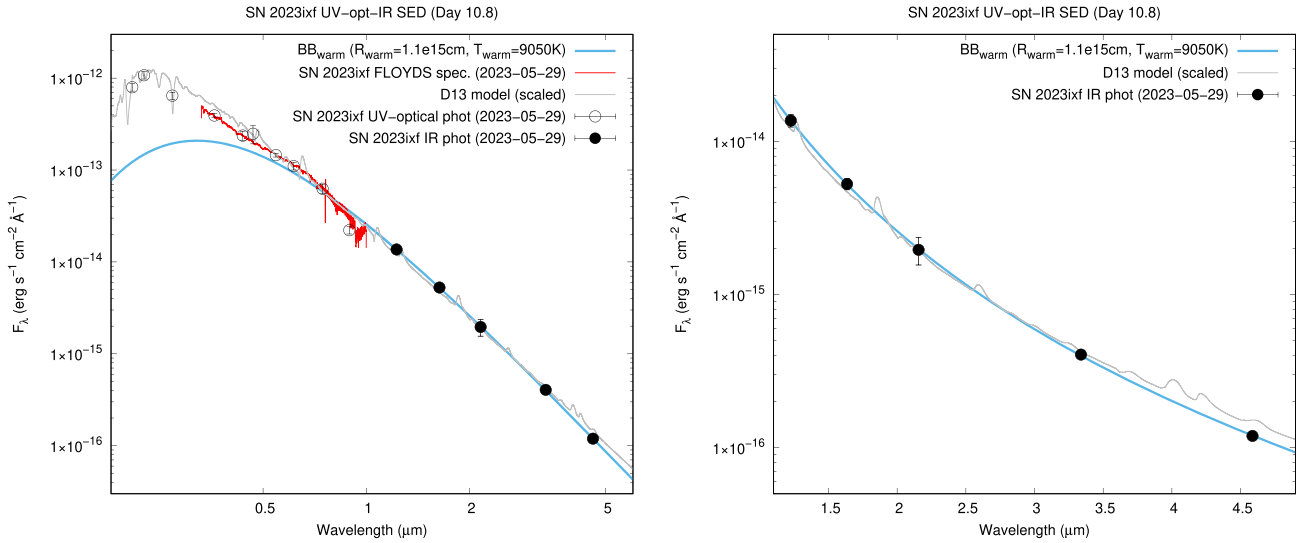

Figure 4. Left: the combined, dereddened UV–optical-IR SED of SN 2023ixf on day 10.8; see text for sources of the photometry. For comparison, we also show a dereddened, renormalized FTN/FLOYDS spectrum from day 10.73 (K. A. Bostroem et al. 2023, red curve). Blackbody fitting of the SED was performed, consisting of only one component (solid blue curve) at $T_{\rm warm} = 9050$ K, with only the near-IR and mid-IR fluxes (filled circles) used in the fitting. The fit is poor for wavelengths <1 μm. A scaled version of the *m15mlt1* model spectrum at day 11 (solid gray curve) from L. Dessart et al. (2013, D13) provides a much better representation of the observed data. The inferred radius of the blackbody is $R_{\rm warm} \approx 1.1 \times 10^{15}$ cm. Right: a zoom-in of just the IR portion of the SED. Note that the D13 model provides an overall reasonable representation of the SED, even for the NEOWISE bands.

blackbody radius is $R_{\rm IR} \approx 2.6 \times 10^{15}$ cm. C. D. Kilpatrick et al. (2023) and S. D. Van Dyk et al. (2024), for example, inferred that the RSG progenitor candidate was surrounded by a dusty shell with an inner radius $R_{\rm in} \approx (0.5\text{–}1.0) \times 10^{15}$ cm. The assumption S. D. Van Dyk et al. (2024) made in their modeling of the star was that the dust shell extended out to $1000 \times R_{\rm in}$, with the dust density declining $\propto r^{-2}$. Furthermore, $\sim$1620 K is roughly the estimated evaporation temperature of $\sim$0.01–0.1 μm-sized silicate-dominated dust in SN environments (e.g., C. Gall et al. 2014). (Note that S. D. Van Dyk et al. 2024 were able to fit the reddening-corrected SED of the pre-explosion dust shell with a simple $\sim$1761 K blackbody.) Thus, we speculate that the IR excess was emanating from within the dusty CSM shell and the SN shock, $R_{\rm shock} < R_{\rm in}$.

This analysis, including the NEOWISE data, lends credence to the overall picture of the progenitor star, inferred via the modeling of the observed SED of the star. The estimated luminosity from the optically thin dust was still about 2 orders of magnitude larger than the luminosity of the progenitor candidate ($\sim 9 \times 10^4\, L_\odot$, or $\sim 3.5 \times 10^{38}$ erg s^{-1}; S. D. Van Dyk et al. 2024), which implies that the dust shell was likely heated by and was reprocessing the UV emission from the interaction of the SN shock with the dense inner CSM. We note that much of the CSM dust was likely destroyed immediately after the explosion by high-energy (extreme UV to γ-ray) photons from the blast through grain sublimation, vaporization, and extreme grain charging effects (A. P. Jones 2004). G. Li et al. (2024) found early indications of CSM dust, with the dust nearest to the explosion likely sublimated within the first few hours.

We built a similar SED from the available UV/optical/near-IR/NEOWISE photometry from day 10.836. Again, we added to this a dereddened and renormalized FTN–FLOYDS-N SN spectrum from WISEReP from 2023 May 29 (K. A. Bostroem et al. 2023). The resulting SED is shown in Figure 4. We attempted to fit a blackbody with $T_{\rm warm} = 9050$ K to the data; however, as can be seen in the figure, while this fit is very good in the IR, it provides a poor fit for wavelengths <1 μm. If we

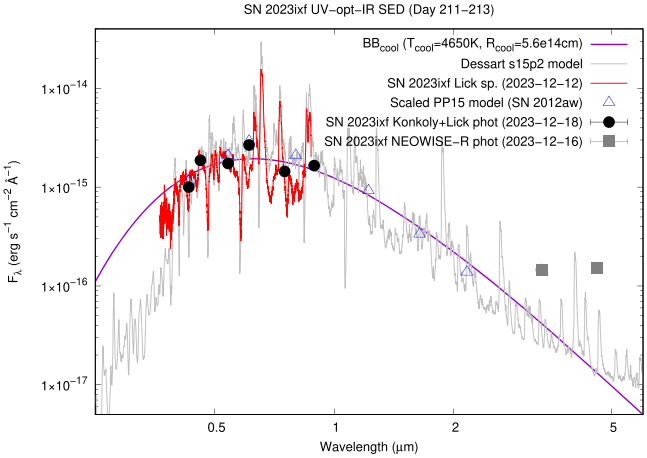

Figure 5. One-component blackbody fit to the days 211–213 optical SED of SN 2023ixf (filled circles). NEOWISE-R data (filled gray squares) were excluded from the fit. Atmospheric models for SNe IIP are also shown for comparison: The day 207 *s15p2* model spectrum (courtesy of Luc Dessart, gray curve) and the distance-scaled model fluxes interpolated between days 193 and 242, for SN 2012aw from O. Pejcha & J. L. Prieto (2015, open blue triangles); the distance to SN 2012aw ($D = 9.9$ Mpc) was adopted from S. Bose et al. (2013).

consider the radiation models for SNe IIP by L. Dessart et al. (2013, D13), specifically, the *m15mlt1* model (with an initial progenitor mass and final progenitor radius of 15 $M_\odot$ and $R_\star = 1$, 107 $R_\odot$, respectively) computed at day 11, that model provides a remarkably good comparison, from the UV through to the mid-IR, with the observed data. This implies that what we were seeing at that epoch, including with NEOWISE, was SN ejecta-dominated emission. If we take into account the blackbody fit, the inferred luminosity is $\gtrsim 5.8 \times 10^{42}$ erg s^{-1}, which is a lower limit, since a significant amount of luminosity is still emerging from the SN at <1 μm. In fact, if we integrate the D13 model (for instance), we obtain a luminosity of $\sim 1.5 \times 10^{43}$ erg s^{-1}. The blackbody radius is $R_{\rm warm} \approx 1.1 \times 10^{15}$ cm. Once again, assuming $v_{\rm exp} = 8000$ km s^{-1}, the shock radius would have been

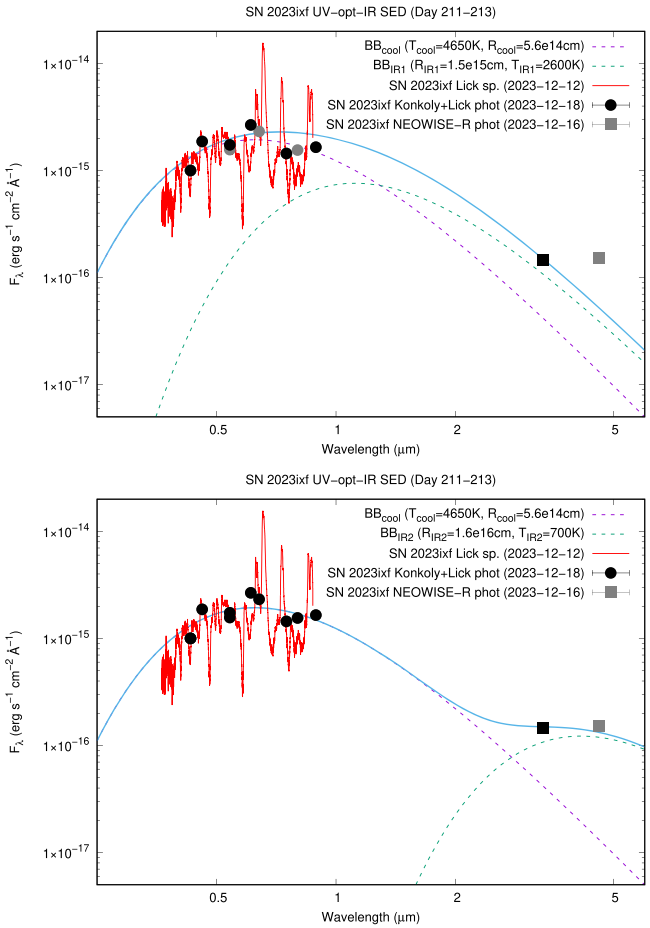

Figure 6. The same as in Figure 5, but with two-component blackbody (BB) fits on the combined days 211–213 optical-IR SED of SN 2023ixf, and without showing atmospheric models. The NEOWISE-R W2 point was excluded from the fit because of the potential contamination by line emission from the CO 1–0 vibrational band. The parameters of the cool component are the same as in Figure 5. The panels show two scenarios for the additional dust component: one calculated assuming the highest theoretical dust temperature ($T_{IR1} = 2600$ K, top panel), and another assuming $T_{IR2} = 700$ K (bottom panel); see details in the text.

$R_{shock} \approx 7.5 \times 10^{14}$ cm, roughly consistent with R_{warm}; similarly to day 3.631, a somewhat higher $v_{exp} = 11,000$ km s^{-1} would result in better agreement between the R_{shock} and R_{warm}.

The blackbody radii and temperatures that we have calculated for both days 3.6 and 10.8 are in good agreement with the results of A. Singh et al. (2024). Note, however, that we have assumed a spherical and homogeneous medium, while early-phase spectropolarimetric data implied the presence of an aspherical dense CSM and a clumpy, low-density extended CSM around SN 2023ixf (S. S. Vasylyev et al. 2023; A. Singh et al. 2024). Nevertheless, our conclusions also fit with that of S. S. Vasylyev et al. (2023) in that those authors concluded that the expanding SN ejecta just emerged from the dense CSM region around day 3.5.

3.2. Late-time Mid-IR Excess

We computed the averages of the various measurements obtained by NEOWISE at late times in the SN's evolution, between MJD 60294.5 and 60296.1. SN 2023ixf was already well on the radioactively powered exponential tail by this point.

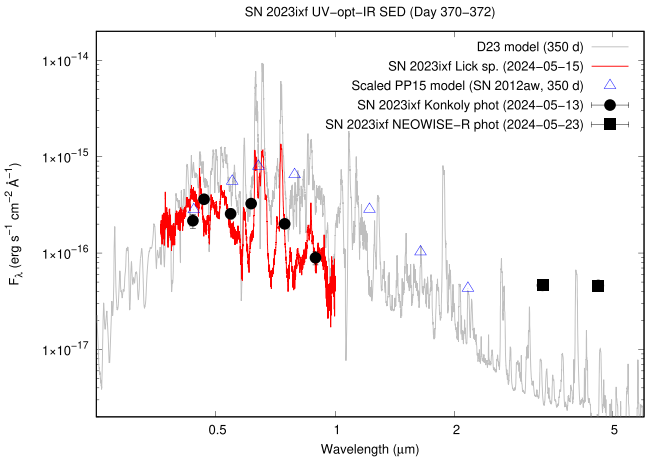

Figure 7. Optical-IR SED of SN 2023ixf from days 370–372. Atmospheric models for SNe IIP are also shown for comparison: The day 350 *s15p2* model spectrum from L. Dessart et al. (2023, D23) and the distance-scaled PP15 models for the same epoch.

The averages are 11.895 ± 0.023 mag and 10.509 ± 0.020 mag in W1 and W2, respectively, with reference to day 213.

Thanks to the active worldwide follow-up observations of SN 2023ixf, we can also build the late-time optical–near-IR SED for the SN. We assembled the unpublished optical *BVgriz* photometry from Konkoly Observatory (from 2023 December 18.5, day 214; J. Vinkó et al. 2024, in preparation) and Lick Observatory *BVRI* data (interpolated to the same date), as well as a single Lick optical spectrum (from 2023 December 12, day 208; W. Zheng et al. 2024, in preparation); see Section 2. We show the combined optical SED in Figure 5. Since we are unaware of any available near-IR data close to this late epoch, we included spectra and fluxes from models of SN IIP explosions for comparison: The day 207 *s15p2* model spectrum courtesy of Luc Dessart and the interpolated and distance-scaled day +193 and +242 model fluxes for the Type IIP SN 2012aw from O. Pejcha & J. L. Prieto (2015). (We compared the Fe II line velocities for SN 2023ixf from W. Zheng et al. 2024, in preparation, to that of SN 2012aw from S. Bose et al. 2013 and found a very good match even at late phases; we also adopted the SN 2012aw distance of 9.9 Mpc from S. Bose et al. 2013.) Both the model spectrum and the set of optical model fluxes appear to compare well with our late-time measured optical data; thus, we find it to be a reasonable approach to use the near-IR components of these models as references during the analysis of the late-time optical-IR SED.

As can be seen in Figure 5, the NEOWISE 3.4 and 4.6 μm data show a clear excess relative to the model fluxes. We fit a single blackbody to the optical–near-IR part of the SED with temperature $T_{cool} = 4650$ K and corresponding radius $R_{cool} = 5.6 \times 10^{14}$ cm. While SN ejecta are not expected to be realistically represented by a blackbody at late epochs, we can then use the result of this fit to provide a characterization of the colder, longer-wavelength excess that is apparent.

As we noted in Section 3.1, we assume that the majority of pre-existing dust grains, located in the dense, confined circumstellar shell, have been evaporated at early times after the explosion; therefore, these likely can no longer be responsible for the excess. Thus, we consider two possible alternate scenarios: (i) At day 213, newly formed dust existed either in the inner (unshocked) ejecta or in the contact discontinuity between the forward and reverse shocks (the

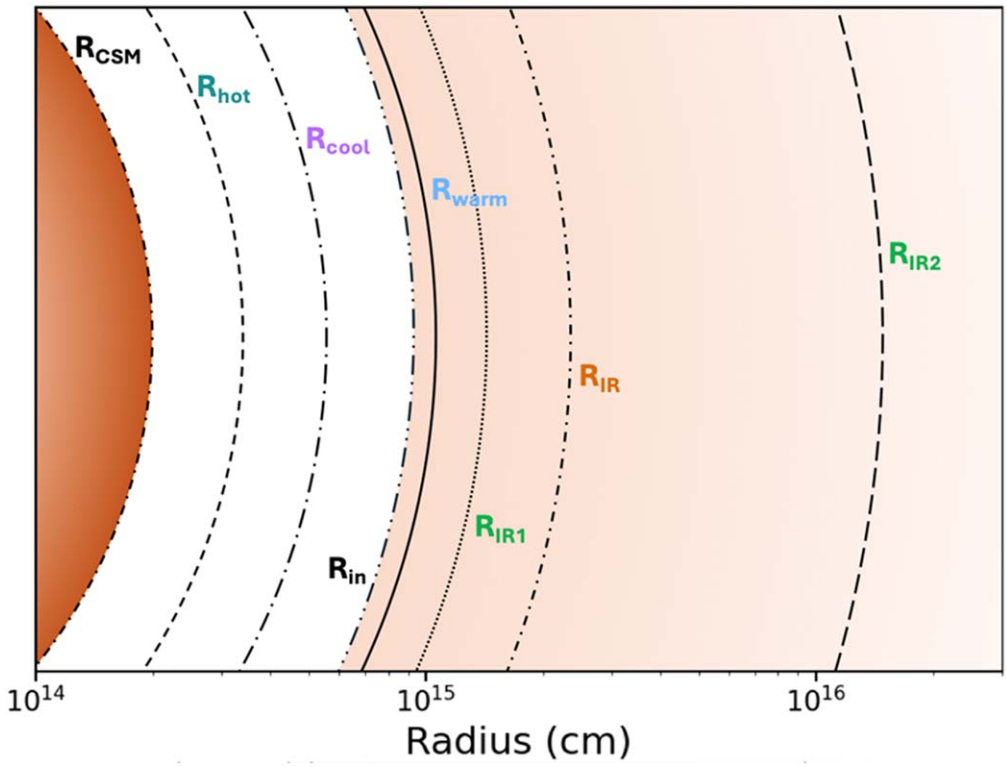

Figure 8. A schematic diagram showing the radii, to approximate scale, at the different NEOWISE-R epochs relative to the pre-SN dense, confined CSM, $R_{\rm CSM}$ (E. A. Zimmerman et al. 2024; the CSM itself is colored dark orange), and the dust shell inner radius, $R_{\rm in}$ (e.g., S. D. Van Dyk et al. 2024; the extended shell is colored light orange). The radii $R_{\rm hot}$ and $R_{\rm IR}$ are from day 3.6; $R_{\rm warm}$ is from day 10.8; and $R_{\rm cool}$, $R_{\rm IR1}$, and $R_{\rm IR2}$ are with respect to days 211–213. See text.

CDS), or (ii) radiation was being emitted by more distant pre-existing dust grains in the SN environment, heated collisionally or radiatively by the (forward) SN shock. However, from only the two mid-IR data points, a detailed investigation of the origin and properties of the assumed late-time dust is challenging to carry out—we hope that pending JWST observations of the SN will provide greater insight into these two scenarios. Furthermore, we note that the large 4.6 μm flux excess at day 213 can also be explained by the emergence of the 1–0 vibrational band of carbon monoxide (CO) at 4.65 μm, as seen in some SNe IIP with observed mid-IR spectra at a similar age (e.g., R. Kotak et al. 2005, 2006; T. Szalai et al. 2011; T. Szalai & J. Vinkó 2013), and also predicted by modeling of exploding RSGs (C. McLeod et al. 2024). The presence of a late-time mid-IR excess is in agreement with the results from A. Singh et al. (2024); they found that the flattening in the K_s-band light curve and the attenuation of the red edge of the Hα line profile $\sim$125 days after the explosion is indicative of the onset of molecular CO and, hence, dust formation in SN 2023ixf. This possibility should also be taken into account during any analysis.

Thus, we also excluded the W2 flux and fit a two-component blackbody model to the remainder of the optical-IR SED, holding the parameters from the cool component fixed. Since a fit to only one mid-IR point would not provide any physically relevant information, we applied temperature constraints and assumed two possible scenarios for the additional dust component: (i) First, we assumed the highest theoretical dust temperature possible for "hot" amorphous carbon dust, $T_{\rm IR1} = 2600$ K (see, e.g., C. Gall et al. 2014); and, (ii) second, we assumed a "typical" temperature of "warm" dust ($T_{\rm IR2} = 700$ K) seen in SNe IIP at a similar age (see, e.g., R. Kotak et al. 2009; T. Szalai et al. 2011; T. Szalai & J. Vinkó 2013). Using these two assumptions, we found blackbody radii of $R_{\rm IR1} \approx 1.5 \times 10^{15}$ cm and $R_{\rm IR2} \approx 1.6 \times 10^{16}$ cm, respectively, for the two assumptions; see Figure 6.

Extrapolating the Fe II velocities (W. Zheng et al. 2024, in preparation) to day 213, we estimated $\sim$1400–1500 km s^{-1} for the ejecta velocity, which results in (2.6–2.8) $\times 10^{15}$ cm for the ejecta radius. This implies that in the case of very high-temperature "hot" dust (the first scenario above), these grains possibly could be within the ejecta. However, assuming a more realistic "warm" dust temperature (the second scenario), the dust would more likely be outside the ejecta. As S. D. Van Dyk et al. (2024) concluded, the dusty shell of the progenitor likely had an inner radius $R_{\rm in} \approx 10^{15}$ cm, with an r^{-2} density distribution extending outward. Thus, the pre-explosion shell itself could easily have extended out to $\sim 1.6 \times 10^{16}$ cm (well beyond the confined volume); the dust we infer here could have been located within the CSM, being either pre-existing or newly formed in the CDS.

We present in Figure 7 an optical-IR SED comprised of data obtained in the day 370–372 interval. Since at that range of epochs, the shape of the measured optical SED appears to differ significantly from SN IIP atmospheric models by either L. Dessart et al. (2023) or O. Pejcha & J. L. Prieto (2015), we are unable to directly estimate the amount of IR excess in the manner that we did for the day 211–213 SED. Nevertheless, clear excesses at both 3.3 and 4.6 μm are again obvious.

For perspective, we provide in Figure 8 a summary schematic diagram showing the various radii we have estimated at the different epochs relative to the dimensions of the progenitor star environment prior to the explosion, specifically the radius of the dense, confined CSM, $R_{\rm CSM}$, and the inner

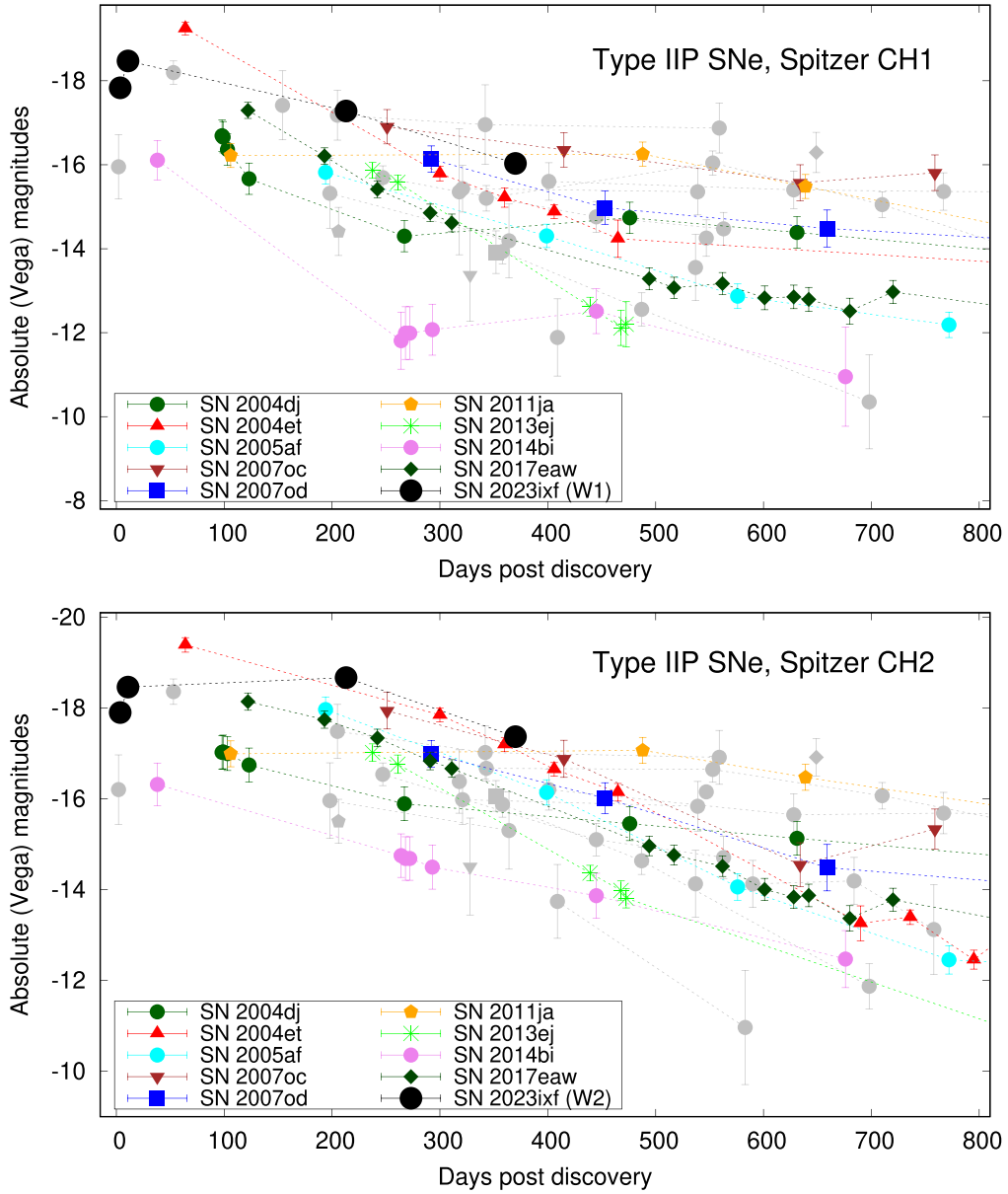

Figure 9. Mid-IR luminosity evolution of SN 2023ixf (NEOWISE W1 and W2 data, filled black circles), compared with Spitzer IRAC data for other SNe II (T. Szalai et al. 2019). Well-sampled objects are highlighted with colored symbols, while all other published detections are marked with gray symbols and are not listed in the figure legend. The earliest gray symbol shown is SN 2009js, at 2 days postexplosion (P. Gandhi et al. 2013; T. Szalai et al. 2019).

radius of the circumstellar dust shell, $R_{\rm in}$: $R_{\rm hot}$ and $R_{\rm IR}$ are with respect to day 3.6; $R_{\rm warm}$ is from day 10.8; and, $R_{\rm cool}$, $R_{\rm IR1}$, and $R_{\rm IR2}$ are with respect to days 211–213. The stellar photosphere was likely at $R_\star \approx 1 \times 10^{14}$ cm (e.g., S. D. Van Dyk et al. 2024).

3.3. Comparison of SN 2023ixf with Other SNe II In the Mid-IR

We have considered all of the NEOWISE data for SN 2023ixf in the context of the mid-IR emission from about 25 other SNe. To achieve this, we compared SN 2023ixf with the sample of SNe from T. Szalai et al. (2019), who presented photometric data obtained by Spitzer in the IR Array Camera (IRAC; G. G. Fazio et al. 2004) bands at 3.6 and 4.5 μm during both the cryogenic and Warm missions; see Figure 9. Most of the well-sampled comparison SNe can be considered as IIP; however, in a similar vein to the SN 2023ixf classification, SN 2007od was considered to be a short-plateau IIP (C. Inserra et al. 2011), as were SN 2011ja (J. E. Andrews et al. 2016) and SN 2013ej (F. Huang et al. 2015; G. Dhungana et al. 2016, however, S. Bose et al. 2015 called this SN a IIL). We note that no SN IIL (other than SN 2013ej, if it can be considered an IIL) has published photometry at these wavelengths during the first ∼500 days after the explosion (the earliest data are for SN 2014G from day ∼570; see T. Szalai et al. 2019). So, SN 2023ixf is in good company here. While the bandpasses for Spitzer IRAC differ slightly from those of NEOWISE W1 and W2 channels, we can draw some basic conclusions.

First, as noted above, SN 2023ixf became the best-observed SN II in the mid-IR during the first several days after the explosion. Second, SN 2023ixf is one of the most luminous SNe II in the mid-IR ever seen. This statement is especially striking, considering the 4.5/4.6 μm photometric evolution of SNe II (Figure 9; right panel)—at day 213, SN 2023ixf is more

luminous than at early times and than any of the other SNe II detected so far at late times. We can speculate on why this is the case. The early-time mid-IR luminosity is consistent with the overall excess observed at other wavelengths and can be explained by the shock-CSM interaction. Among the Spitzer sample, most of the SNe were either of low luminosity (e.g., SN 2004dj) or were otherwise normal (e.g., SN 2005af, SN 2007oc, SN 2014bi); SN 2004et, for instance, was observed to be somewhat extraordinary (e.g., K. Maguire et al. 2010, see also M. Shahbandeh et al. 2023). The late-time mid-IR excess for SN 2023ixf could be due to postexplosion dust formation, as we have mentioned above. However, we cannot say much more about this, based on the NEOWISE data alone; observations with JWST will likely provide significantly more insight on this.

4. Conclusions

We have analyzed serendipitous observations of SN 2023ixf made as part of routine NEOWISE survey scanning operations, starting on day 3.6 through day 10.9 after the explosion and again at late times from days 211 through 213 and days 370 through 372. For the three epochs in these time ranges that we analyzed, we combined the NEOWISE observations with data from the UV through the near-IR whenever possible. At day 3.6, we approximated the emission in the optical with a hot, $\sim$26,630 K blackbody, exhibiting a marked excess in the UV, likely resulting from strong, early SN shock-CSM interaction. In the IR, however, a definite excess is also obvious, and we fit that with a cooler, $\sim$1620 K blackbody with a radius of $\sim 2.6 \times 10^{15}$ cm. We concluded that this is consistent with dust in an inferred circumstellar shell surrounding the progenitor star having been heated by the UV emission from the early CSM interaction. On day 10.8, the emission, including that detected with NEOWISE, was consistent with being SN ejecta dominated.

At late times we also observed an obvious excess in the NEOWISE bands, relative to the other wavelengths. This excess could arise either from newly formed dust in the inner ejecta or in the contact discontinuity between the forward and reverse shocks (the CDS), or from more distant pre-existing dust grains in the SN environment. Furthermore, the observed large excess at 4.6 μm at late times can also be explained by the emergence of the CO 1–0 vibrational band, seen in some SNe IIP. Observations with JWST are necessary to confirm the detection of the CO band, as well as to better explore the overall nature of the late-time mid-IR emission.

We found, from comparing to mid-IR data for other SNe II, that SN 2023ixf is the best-observed SN II in the mid-IR during the first several days after the explosion and one of the most luminous SNe II ever seen in the mid-IR. The survey operations by the WISE mission, in all its incarnations, were terminated permanently on 2024 July 31. Together with the decommissioning of Spitzer over 4 yr ago, the number of available facilities to gather mid-IR light from nearby SNe are now greatly diminished. The next avenue will be provided by NEO Surveyor, set for launch no later than mid-2028 (A. K. Mainzer et al. 2023). The mission will be obtaining four detections at 4.6 and 8 μm over a 6 hr time period, approximately every 13 days, as part of survey operations, so it may be possible once again to catch SNe both on the rise and at late times. For future pointed observations, it falls on JWST to be the platform for observing both new and old SNe to explore further in detail the nature of dust associated with these spectacular events.

Acknowledgments

We thank the reviewer for their helpful comments, which improved the manuscript. We are grateful to Luc Dessart for providing the day 207 model SN IIP spectrum. This publication makes use of data products from the Near-Earth Object Wide-field Infrared Survey Explorer, which is a joint project of the Jet Propulsion Laboratory/California Institute of Technology and the University of Arizona. It also uses data products from the Wide-field Infrared Survey Explorer, which is a joint project of the University of California, Los Angeles, and the Jet Propulsion Laboratory/California Institute of Technology. WISE and NEOWISE are funded by NASA. This work has been supported by the GINOP-2-3-2-15-2016-00033 project of the National Research, Development and Innovation (NRDI) Office of Hungary, funded by the European Union, as well as by NKFIH OTKA FK-134432, KKP-143986, and K-142534 grants, and from the HUN-REN Hungarian Research Network. L.K. and K.V. are supported by the Bolyai János Research Scholarship of the Hungarian Academy of Sciences. L.K. acknowledges the Hungarian National Research, Development, and Innovation Office grant OTKA PD-134784. The authors acknowledge financial support of the Austrian-Hungarian Action Foundation grants 98öu5, 101öu13, 112öu1. A.V.F.'s research group at the University of California, Berkeley acknowledges financial assistance from the Christopher R. Redlich Fund, Gary and Cynthia Bengier, Clark and Sharon Winslow, Alan Eustace (W.Z. is a Bengier–Winslow–Eustace Specialist in Astronomy), William Draper, Timothy and Melissa Draper, Briggs and Kathleen Wood, Sanford Robertson (T.G.B. is a Draper–Wood–Robertson Specialist in Astronomy), and numerous other donors. KAIT and its ongoing operation at Lick Observatory were made possible by donations from Sun Microsystems, Inc., the Hewlett-Packard Company, AutoScope Corporation, Lick Observatory, the U.S. NSF, the University of California, the Sylvia and Jim Katzman Foundation, and the TABASGO Foundation. A major upgrade of the Kast spectrograph on the Shane 3 m telescope at Lick Observatory, led by Brad Holden, was made possible through generous gifts from the Heising-Simons Foundation, William and Marina Kast, and the University of California Observatories. Many UC Berkeley undergraduate students helped obtain the Lick 1 m Nickel data, especially Kate Bostow, Asia de Graw, Eli Gendreau-Distler, Connor Jennings, and Neil Pichay. We appreciate the excellent assistance of the staff at Lick Observatory. Research at Lick Observatory is partially supported by a generous gift from Google.

Facilities: NEOWISE, KAIT, Nickel, Shane, IRSA, RC80 (Konkoly).

Software: IRAF (D. Tody 1986, 1993), PyRAF (http://www.stsci.edu/institute/software_hardware/pyraf), `ICORE` (https://irsa.ipac.caltech.edu/applications/ICORE/; doi:10.26131/IRSA535).

Appendix
Pre-explosion NEOWISE Nondetections

As pointed out in Section 2.1, NEOWISE obtained pre-explosion observations of the SN site between 2013 December 18 and 2022 December 18, with the last pair of single exposures occurring 150.75 d prior to the explosion. The progenitor candidate was not detected in any of these exposures. A deep stack of all of these exposures in each of

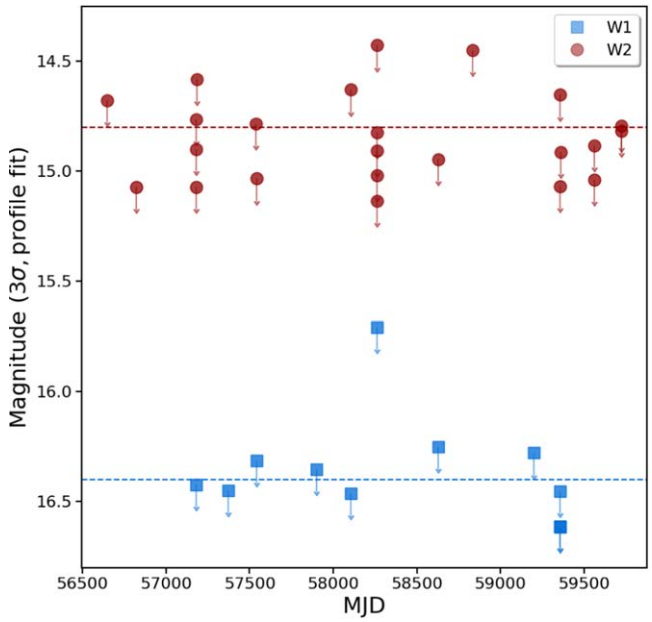

Figure 10. Estimates of the NEOWISE-R 3σ upper limits on the detection of the SN 2023ixf progenitor candidate from between 2013 December and 2022 December at 3.4 and 4.6 μm (bands W1 and W2, respectively). Also shown are the mean values for the data at both bands (dashed lines). The observed magnitudes shown are in the Vega system. These have not been reddening corrected.

the bands made with ICORE[18] is shown in Figure 1. Nothing is perceptible at the SN site in these mosaics. As S. D. Van Dyk et al. (2024) described, estimates of the upper limits on detection were established by isolating in the NEOWISE-R Single Exposure Source Table, obtained from IRSA, all of the 3σ detected objects within 60″ of the SN position for each band. We show these upper limits in Figure 10. Both the mean and median values in W1 are <16.4 mag; the mean value in W2 is <14.8 mag, whereas the median value is <14.9 mag.

ORCID iDs

Schuyler D. Van Dyk https://orcid.org/0000-0001-9038-9950
Tamás Szalai https://orcid.org/0000-0003-4610-1117
Roc M. Cutri https://orcid.org/0000-0002-0077-2305
J. Davy Kirkpatrick https://orcid.org/0000-0003-4269-260X
Carl J. Grillmair https://orcid.org/0000-0003-4072-169X
Sergio B. Fajardo-Acosta https://orcid.org/0000-0001-9309-0102
Joseph R. Masiero https://orcid.org/0000-0003-2638-720X
Amy K. Mainzer https://orcid.org/0000-0002-7578-3885
Christopher R. Gelino https://orcid.org/0000-0001-5072-4574
József Vinkó https://orcid.org/0000-0001-8764-7832
András Péter Joó https://orcid.org/0000-0001-5203-434X
András Pál https://orcid.org/0000-0001-5449-2467
Réka Könyves-Tóth https://orcid.org/0000-0002-8770-6764
Róbert Szakáts https://orcid.org/0000-0002-1698-605X
Krisztián Vida https://orcid.org/0000-0002-6471-8607
WeiKang Zheng https://orcid.org/0000-0002-2636-6508
Thomas G. Brink https://orcid.org/0000-0001-5955-2502
Alexei V. Filippenko https://orcid.org/0000-0003-3460-0103

[18] https://irsa.ipac.caltech.edu/applications/ICORE/

References

Anderson, J. P., González-Gaitán, S., Hamuy, M., et al. 2014, ApJ, 786, 67
Andrews, J. E., Gallagher, J. S., Clayton, G. C., et al. 2010, ApJ, 715, 541
Andrews, J. E., Krafton, K. M., Clayton, G. C., et al. 2016, MNRAS, 457, 3241
Andrews, J. E., Sugerman, B. E. K., Clayton, G. C., et al. 2011, ApJ, 731, 47
Arendt, R. G., Dwek, E., Kober, G., Rho, J., & Hwang, U. 2014, ApJ, 786, 55
Barbon, R., Ciatti, F., & Rosino, L. 1979, A&A, 72, 287
Barlow, M. J., Krause, O., Swinyard, B. M., et al. 2010, A&A, 518, L138
Berger, E., Keating, G. K., Margutti, R., et al. 2023, ApJL, 951, L31
Bose, S., Kumar, B., Sutaria, F., et al. 2013, MNRAS, 433, 1871
Bose, S., Sutaria, F., Kumar, B., et al. 2015, ApJ, 806, 160
Bostroem, K. A., Pearson, J., Shrestha, M., et al. 2023, ApJL, 956, L5
Bostroem, K. A., Sand, D. J., Dessart, L., et al. 2024, ApJL, 973, L47
Bouchet, P., Dwek, E., Danziger, J., et al. 2006, ApJ, 650, 212
Cernuschi, F., & Codina, S. 1967, AJ, 72, 788
Chambers, K. C., Magnier, E. A., Metcalfe, N., et al. 2016, arXiv:1612.05560
Chandra, P., Chevalier, R. A., Maeda, K., Ray, A. K., & Nayana, A. J. 2024, ApJL, 963, L4
De Looze, I., Barlow, M. J., Bandiera, R., et al. 2019, MNRAS, 488, 164
Dessart, L., Gutiérrez, C. P., Kuncarayakti, H., Fox, O. D., & Filippenko, A. V. 2023, A&A, 675, A33
Dessart, L., & Hillier, D. J. 2022, A&A, 660, L9
Dessart, L., Hillier, D. J., Waldman, R., & Livne, E. 2013, MNRAS, 433, 1745
Dhungana, G., Kehoe, R., Vinko, J., et al. 2016, ApJ, 822, 6
Dong, Y., Sand, D. J., Valenti, S., et al. 2023, ApJ, 957, 28
Dwek, E., Arendt, R. G., Bouchet, P., et al. 2010, ApJ, 722, 425
Dwek, E., Galliano, F., & Jones, A. P. 2007, ApJ, 662, 927
Dwek, E., Sarangi, A., & Arendt, R. G. 2019, ApJL, 871, L33
Fabbri, J., Otsuka, M., Barlow, M. J., et al. 2011, MNRAS, 418, 1285
Fazio, G. G., Hora, J. L., Allen, L. E., et al. 2004, ApJS, 154, 10
Filippenko, A. V. 1997, ARA&A, 35, 309
Fitzpatrick, E. L. 1999, PASP, 111, 63
Fox, O. D., Chevalier, R. A., Dwek, E., et al. 2010, ApJ, 725, 1768
Fox, O. D., Chevalier, R. A., Skrutskie, M. F., et al. 2011, ApJ, 741, 7
Fox, O. D., Filippenko, A. V., Skrutskie, M. F., et al. 2013, AJ, 146, 2
Gall, C., Hjorth, J., & Andersen, A. C. 2011, A&AR, 19, 43
Gall, C., Hjorth, J., Watson, D., et al. 2014, Natur, 511, 326
Gal-Yam, A. 2017, in Handbook of Supernovae, ed. A. W. Alsabti & P. Murdin (Berlin: Springer), 195
Gandhi, P., Yamanaka, M., Tanaka, M., et al. 2013, ApJ, 767, 166
Gomez, H. L., Krause, O., Barlow, M. J., et al. 2012, ApJ, 760, 96
Grefenstette, B. W., Brightman, M., Earnshaw, H. P., Harrison, F. A., & Margutti, R. 2023, ApJL, 952, L3
Hiramatsu, D., Howell, D. A., Moriya, T. J., et al. 2021, ApJ, 913, 55
Hiramatsu, D., Tsuna, D., Berger, E., et al. 2023, ApJL, 955, L8
Hosseinzadeh, G., Farah, J., Shrestha, M., et al. 2023, ApJL, 953, L16
Hoyle, F., & Wickramasinghe, N. C. 1970, Natur, 226, 62
Hsu, B., Smith, N., Goldberg, J. A., et al. 2024, arXiv:240807874H
Huang, F., Wang, X., Zhang, J., et al. 2015, ApJ, 807, 59
Indebetouw, R., Matsuura, M., Dwek, E., et al. 2014, ApJL, 782, L2
Inserra, C., Turatto, M., Pastorello, A., et al. 2011, MNRAS, 417, 261
Itagaki, K. 2023, TNSTR, 2023-39, 1
Jacobson-Galán, W. V., Dessart, L., Margutti, R., et al. 2023, ApJL, 954, L42
Jencson, J. E., Kasliwal, M. M., Adams, S. M., et al. 2019, ApJ, 886, 40
Jencson, J. E., Pearson, J., Beasor, E. R., et al. 2023, ApJL, 952, L30
Jones, A. P. 2004, in ASP Conf. Ser. 309, Astrophysics of Dust, ed. A. N. Witt et al. (San Francisco, CA: ASP), 347
Kasliwal, M. M., Bally, J., Masci, F., et al. 2017, ApJ, 839, 88
Kilpatrick, C. D., Foley, R. J., Jacobson-Galán, W. V., et al. 2023, ApJL, 952, L23
Kokubo, M., Mitsuda, K., Morokuma, T., et al. 2019, ApJ, 872, 135
Kotak, R., Meikle, P., Pozzo, M., et al. 2006, ApJL, 651, L117
Kotak, R., Meikle, P., Van Dyk, S. D., Höflich, P. A., & Mattila, S. 2005, ApJL, 628, L123
Kotak, R., Meikle, W. P. S., Farrah, D., et al. 2009, ApJ, 704, 306
Li, G., Hu, M., Li, W., et al. 2024, Natur, 627, 754
Maguire, K., Di Carlo, E., Smartt, S. J., et al. 2010, MNRAS, 404, 981
Mainzer, A., Bauer, J., Cutri, R. M., et al. 2014, ApJ, 792, 30
Mainzer, A., Bauer, J., Grav, T., et al. 2011, ApJ, 731, 53
Mainzer, A. K., Masiero, J. R., Abell, P. A., et al. 2023, PSJ, 4, 224
Martinez, L., Bersten, M. C., Folatelli, G., Orellana, M., & Ertini, K. 2024, A&A, 683, A154
Matsuura, M., De Buizer, J. M., Arendt, R. G., et al. 2019, MNRAS, 482, 1715
Matsuura, M., Dwek, E., Meixner, M., et al. 2011, Sci, 333, 1258
McLeod, C., Hillier, D. J., & Dessart, L. 2024, MNRAS, 532, 549
Meikle, W. P. S., Kotak, R., Farrah, D., et al. 2011, ApJ, 732, 109

Meikle, W. P. S., Mattila, S., Pastorello, A., et al. 2007, ApJ, 665, 608
Moran, S., Fraser, M., Kotak, R., et al. 2023, A&A, 669, A51
NEOWISE Team 2020, NEOWISE-R Single Exposure (L1b) Source Table, IPAC, doi:10.26131/IRSA144
Pejcha, O., & Prieto, J. L. 2015, ApJ, 799, 215
Perley, D. A., Fremling, C., Sollerman, J., et al. 2020, ApJ, 904, 35
Perley, D. A., Gal-Yam, A., Irani, I., & Zimmerman, E. 2023, TNSAN, 119, 1
Pledger, J. L., & Shara, M. M. 2023, ApJL, 953, L14
Riess, A. G., Yuan, W., Macri, L. M., et al. 2022, ApJL, 934, L7
Sarangi, A. 2022, A&A, 668, A57
Schlegel, E. M. 1996, AJ, 111, 1660
Shahbandeh, M., Sarangi, A., Temim, T., et al. 2023, MNRAS, 523, 6048
Sibthorpe, B., Ade, P. A. R., Bock, J. J., et al. 2010, ApJ, 719, 1553
Singh, A., Teja, R. S., Moriya, T. J., et al. 2024, ApJ, 975, 132
Smartt, S. J. 2015, PASA, 32, e016
Smartt, S. J., Eldridge, J. J., Crockett, R. M., & Maund, J. R. 2009, MNRAS, 395, 1409
Smith, N., Pearson, J., Sand, D. J., et al. 2023, ApJ, 956, 46
Soraisam, M. D., Szalai, T., Van Dyk, S. D., et al. 2023, ApJ, 957, 64
Sugerman, B. E. K., Ercolano, B., Barlow, M. J., et al. 2006, Sci, 313, 196
Sun, L., Xiao, L., & Li, G. 2022, MNRAS, 513, 4057
Szalai, T., Fox, O. D., Arendt, R. G., et al. 2021, ApJ, 919, 17
Szalai, T., & Vinkó, J. 2013, A&A, 549, A79
Szalai, T., Vinkó, J., Balog, Z., et al. 2011, A&A, 527, A61
Szalai, T., Zsíros, S., Fox, O. D., Pejcha, O., & Müller, T. 2019, ApJS, 241, 38
Tartaglia, L., Pastorello, A., Sollerman, J., et al. 2020, A&A, 635, A39
Teja, R. S., Singh, A., Basu, J., et al. 2023, ApJL, 954, L12
Teja, R. S., Singh, A., Sahu, D. K., et al. 2022, ApJ, 930, 34
Temim, T., & Dwek, E. 2013, ApJ, 774, 8
Tinyanont, S., Kasliwal, M. M., Fox, O. D., et al. 2016, ApJ, 833, 231
Tody, D. 1986, Proc. SPIE, 627, 733
Tody, D. 1993, in ASP Conf. Ser. 52, Astronomical Data Analysis Software and Systems II, ed. R. J. Hanisch et al. (San Francisco, CA: ASP), 173
Tonry, J. L., Stubbs, C. W., Lykke, K. R., et al. 2012, ApJ, 750, 99
Valenti, S., Howell, D. A., Stritzinger, M. D., et al. 2016, MNRAS, 459, 3939
Van Dyk, S. D. 2013, AJ, 145, 118
Van Dyk, S. D. 2017, RSPTA, 375, 20160277
Van Dyk, S. D., Srinivasan, S., Andrews, J. E., et al. 2024, ApJ, 968, 27
Vasylyev, S. S., Yang, Y., Filippenko, A. V., et al. 2023, ApJL, 955, L37
Wang, L., Hu, M., Wang, L., et al. 2024, NatAs, 8, 504
Wang, S., & Chen, X. 2019, ApJ, 877, 116
Wesson, R., Barlow, M. J., Matsuura, M., & Ercolano, B. 2015, MNRAS, 446, 2089
Wright, E. L., Eisenhardt, P. R. M., Mainzer, A. K., et al. 2010, AJ, 140, 1868
Yamanaka, M., Fujii, M., & Nagayama, T. 2023, PASJ, 75, L27
Yang, Y.-P., Liu, X., Pan, Y., et al. 2024, ApJ, 969, 126
Yaron, O., & Gal-Yam, A. 2012, PASP, 124, 668
Zimmerman, E. A., Irani, I., Chen, P., et al. 2024, Natur, 627, 759
Zsíros, S., Nagy, A. P., & Szalai, T. 2022, MNRAS, 509, 3235
Zsíros, S., Szalai, T., De Looze, I., et al. 2024, MNRAS, 529, 155